Journal of Applied Physics

Probing thermal conductivity of subsurface, amorphous layers in irradiated diamond

Cite as: J. Appl. Phys. **129**, 055307 (2021); https://doi.org/10.1063/5.0038972
Submitted: 28 November 2020 . Accepted: 12 January 2021 . Published Online: 02 February 2021

Ethan A. Scott, Jeffrey L. Braun, Khalid Hattar, Joshua D. Sugar, John T. Gaskins, Mark Goorsky, Sean W. King, and Patrick E. Hopkins

Journal of Applied Physics ARTICLE scitation.org/journal/jap

Probing thermal conductivity of subsurface, amorphous layers in irradiated diamond

Cite as: J. Appl. Phys. **129**, 055307 (2021); doi: 10.1063/5.0038972
Submitted: 28 November 2020 · Accepted: 12 January 2021 ·
Published Online: 2 February 2021

Ethan A. Scott,[1,2] Jeffrey L. Braun,[1] Khalid Hattar,[2] Joshua D. Sugar,[3] John T. Gaskins,[1] Mark Goorsky,[4] Sean W. King,[5] and Patrick E. Hopkins[1,6,7,a)]

AFFILIATIONS

[1]Department of Mechanical and Aerospace Engineering, University of Virginia, Charlottesville, Virginia 22904, USA
[2]Sandia National Laboratories, Albuquerque, New Mexico 87185, USA
[3]Sandia National Laboratories, Livermore, California 94550, USA
[4]Department of Materials Science and Engineering, University of California Los Angeles, Los Angeles, California 90095, USA
[5]Logic Technology Development, Intel Corporation, Hillsboro, Oregon 97124, USA
[6]Department of Materials Science and Engineering, University of Virginia, Charlottesville, Virginia 22904, USA
[7]Department of Physics, University of Virginia, Charlottesville, Virginia 22904, USA

[a)]**Author to whom correspondence should be addressed:** phopkins@virginia.edu

ABSTRACT

In this study, we report on the thermal conductivity of amorphous carbon generated in diamond via nitrogen ion implantation (N^{3+} at 16.5 MeV). Transmission electron microscopy techniques demonstrate amorphous band formation about the longitudinal projected range, localized approximately 7 μm beneath the sample surface. While high-frequency time-domain thermoreflectance measurements provide insight into the thermal properties of the near-surface preceding the longitudinal projected range depth, a complimentary technique, steady-state thermoreflectance, is used to probe the thermal conductivity at depths which could not otherwise be resolved. Through measurements with a series of focusing objective lenses for the laser spot size, we find the thermal conductivity of the amorphous region to be approximately 1.4 W m^{-1} K^{-1}, which is comparable to that measured for amorphous carbon films fabricated through other techniques.

I. INTRODUCTION

Thermoreflectance techniques such as time-domain thermoreflectance (TDTR) are well-suited for the characterization of the thermal transport properties of thin films and interfaces given the high spatial resolution and non-destructive nature of the measurement.[1–3] Generally, a pulsed laser modulated at high frequency is used to induce a periodic heating event at a sample surface, and the corresponding change in reflectivity is monitored with a secondary probe laser. High modulation frequencies and small laser spot sizes enable the measurement of localized, near-surface features such as thermal resistances attributed to interfaces and thin films.[4–7] As a consequence of high-frequency modulation, however, the ability to measure features beneath the near-surface is limited, as the depth of thermal penetration is inversely related to the modulation frequency and further reduced for materials with low thermal diffusivity.[8–10]

In the other extreme, at frequencies low enough to achieve steady-state heating within the material, the depth of thermal penetration is no longer restricted by the thermal properties (i.e., thermal conductivity or heat capacity)[2,9] but varies proportionally with the radius of the heating laser, which enables the measurement of properties buried deep within the material. In this study, we demonstrate the utility of steady-state thermoreflectance (SSTR) to measure the thermal conductivity of a thin amorphous layer embedded several micrometers beneath the surface of ion-implanted diamond.

The results of this study not only demonstrate the ability of SSTR in measuring the thermal resistance of subsurface layers and interfaces, but also report on the thermal conductivity of amorphous carbon formed via the ion irradiation of crystalline diamond. The former marks an advance in experimental metrology in demonstrating SSTR as a suitable technique to measure the

thermal properties of subsurface thin films. The latter contributes to our fundamental understating of vibrational thermal transport in ion irradiated solids in the disordered layers about the average ion termination depth (i.e., the longitudinal projected range).

The localized nature of damage that can be achieved in crystals at the longitudinal projected range through ion implantation offers an ideal platform to test the capabilities of SSTR as distinct amorphous layers can be produced by ions at sufficiently high fluences. This depth can be tuned based on a number of parameters, including the energy and species of the ion, and thus, we design an experiment in which we ion implant polycrystalline diamond with N^{3+} so that the end of range is at a distance under the surface that is inaccessible with TDTR, but accessible for the measurement with SSTR.

A single-side polished polycrystalline diamond sample, commercially available from Element Six (TM200), was selected as the target medium in order to produce regions of localized amorphization about the projected range, which has been previously demonstrated in diamond for ions with sufficient energy.[11–14] Localization of damage through ion implantation can be represented with the Stopping and Range of Ions in Matter (SRIM) software[15,16] through simulation of the ion concentration and displacements-per-atom (dpa) profiles. An example is provided in Fig. 1(a), which displays the result of diamond implanted with N^{3+} at 16.5 MeV. For this calculation, we utilize a full damage cascade, with nitrogen as the selected ion, and carbon as the target. The carbon target is modified such that its properties are reflective of diamond:[11] density of 3.51 g cm^{-3}, displacement energy of 37.5 eV,[17,18] lattice binding energy of 7.5 eV,[19–21] and a surface binding energy of 3.69 eV.[22,23] The dpa is calculated from the vacancy output of the calculation, assuming a fluence of 4×10^{16} cm^{-3}. As can be seen from Fig. 1(a), the ion concentration and dpa associated with these implant conditions yield profiles that are localized about the longitudinal projected range, with limited longitudinal straggle. In comparison, other materials, such as silicon, will yield amorphous regions in response to implantation with heavy ions but with more spatially diffuse damage profiles.[24,25] The unique localization of damage about the longitudinal projected range in diamond has allowed for advanced lift-out techniques [via focused ion beam (FIB) milling] of the material above the projected range, which leverages the differences in mechanical properties between diamond and amorphous carbon.[14,26,27]

II. EXPERIMENTAL

Ion implantation was carried out at Sandia National Laboratories with a 6 MV Tandem Van de Graaff accelerator. The diamond was adhered with a conductive carbon tape onto a silicon substrate and loaded into the implant chamber that was pumped to 1×10^{-6} Torr. The diamond was subsequently exposed, at normal incidence, to a fluence of 4×10^{16} cm^{-2} N^{3+}. To provide for spatial uniformity during the implantation, the beam was rastered across the sample surface.

Localization of damage from the N^{3+} implantation is confirmed through high angle annular dark field scanning transmission electron microscopy (HAADF STEM) imaging of a cross section of the sample produced from an FEI Titan electron microscope. Figure 1(b) displays a visibly darker region beginning at a depth of 7.03 μm from the sample surface; a higher resolution image of the region is provided in Fig. 1(c). We note that the longitudinal projected range observed from STEM is slightly larger than that predicted through SRIM simulation, which could be attributed to the fact that the crystalline structure and dynamic changes in composition are not accounted for in the model.[28–30] Selected area electron diffraction is used to validate crystallinity of the region, where diffraction is observed directly outside of the region, but

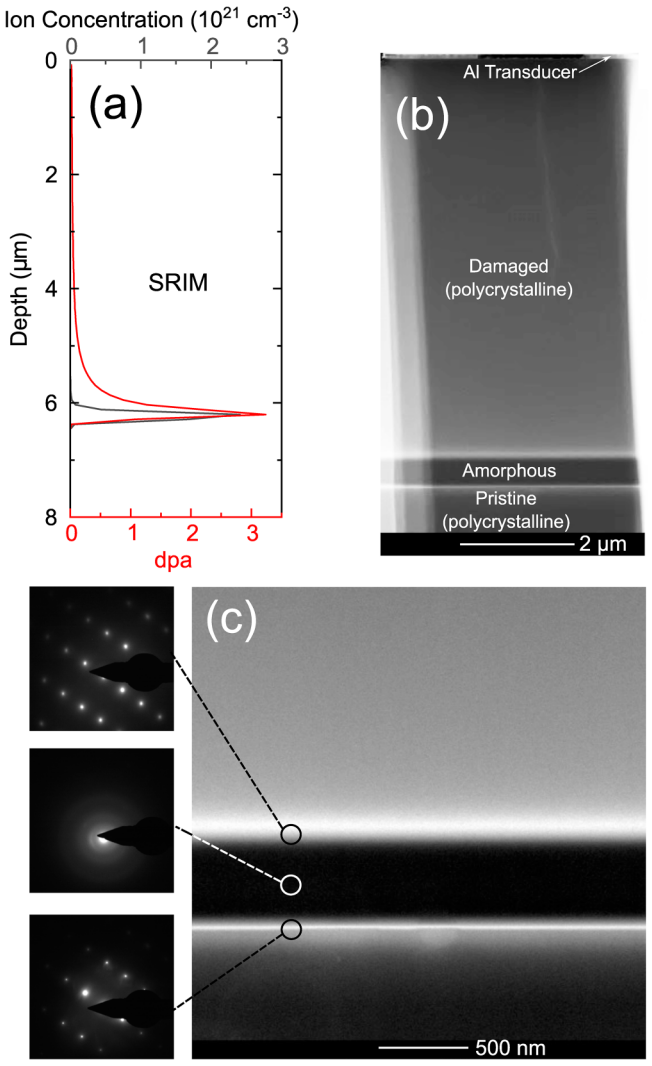

FIG. 1. (a) SRIM simulations of the ion concentration (gray) and dpa profile (red) for N^{3+} implanted diamond, exposed to a dose of 4×10^{16} cm^{-2} and ion energy of 16.5 MeV. (b) and (c) HAADF STEM images of a cross section of the implanted diamond with the same conditions from the SRIM simulation. (c) displays a higher resolution image centered about the longitudinal projected range. The dark band at the projected range is amorphous, confirmed by the lack of diffraction in selected area diffraction measurements. The images in (b) and (c) are included from the previous study.[11] Reproduced with permission from Scott *et al.*, Carbon **157**, 97–105 (2020). Copyright 2020 Elsevier.

within the region itself there is a lack of diffraction, demonstrating the damage levels were sufficient to result in amorphization.

For thermal property characterization of the diamond, both TDTR and SSTR are employed. Both are optical pump-probe techniques in which a modulated heating event is induced with a pump laser that is then monitored with a secondary, reflected probe beam. Samples are coated in a metal film to serve as an opto-thermal transducer, in this case, 80 nm aluminum. The change in reflectance of the sample surface is monitored by a photodetector connected to a lock-in amplifier that is locked-in to the modulation frequency of the pump beam. While TDTR makes use of a pulsed probe and pump modulated at high frequency (up to 10 MHz) and measures the change in reflectivity as a function of time delay between the impingement of pump and probe pulse, SSTR utilizes a continuous wave laser mechanically chopped at low frequency (tens to hundreds of Hertz) to heat the sample to steady-state and measures the change in reflectance as a function of probe power. Examples of characteristic SSTR data from the N^{3+} implanted diamond are displayed in Fig. 2, where it can be seen that the change in reflectivity (which is directly proportional to the signal measured by the photodetector, ΔV/V) is linearly related to the power of the pump. Furthermore, it is also observed that as spot sizes become larger (for smaller-magnification objective lenses), more power is required to produce the same level of measured reflectance.

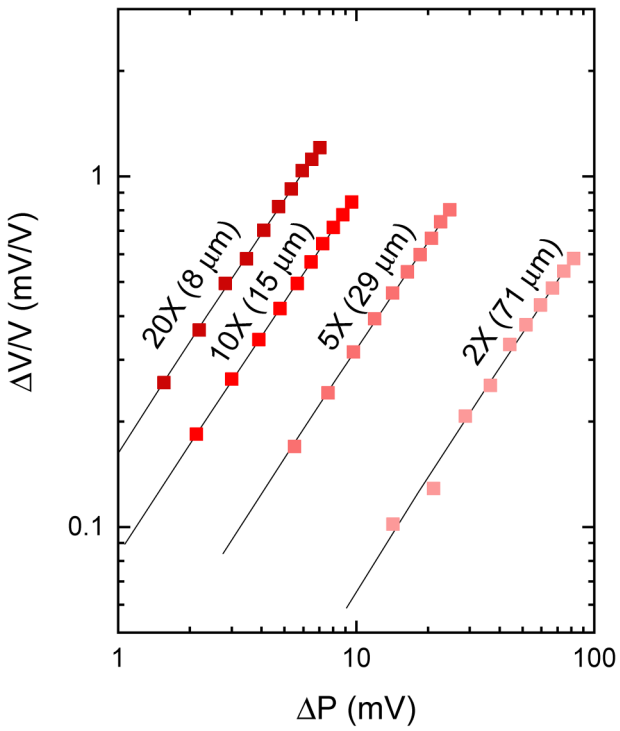

FIG. 2. Example data from SSTR measurements of the ion-implanted diamond, which provides the change in the normalized probe signal as a function of change in ∝pump power. The corresponding objective magnification is labeled beside each dataset in addition to the nominal value for the effective spot size in parentheses. Measurements utilizing larger spot sizes require greater pump powers to achieve the same change in measured reflectivity.

III. RESULTS AND DISCUSSION

To measure the thermal conductivity of the diamond, TDTR is first employed, utilizing a modulation frequency of 8.8 MHz and pulsed probe and pump beams with central wavelengths of 800 and 400 nm, respectively. The spot sizes of the beams are varied by utilizing focusing objectives of 20×-2× magnification, which provides for an effective spot size ($\sqrt{r_0^2 + r_1^2}$ where r_0 and r_1 are the pump and probe radii, respectively) ranging from 5.4 to 44 μm. For each effective spot size, the raw data from the TDTR measurement are fit with a multi-layer heat diffusion equation for which the parameters of interest, including the thermal conductivity (κ) and thermal boundary conductance (G), are treated as fitting parameters.[1,3]

Due to the high modulation frequency of the TDTR measurement, the system is first considered as a two-layer model consisting of an 80 nm Al transducer atop a damaged diamond substrate. It can be seen in Fig. 3 that for each effective spot size, the resultant measured thermal conductivity is within error of the other spot sizes and provides for an average measured thermal conductivity of $26.8 \pm 2.1\ \mathrm{W\,m^{-1}\,K^{-1}}$. At high modulation frequencies, f, the 1/e thermal penetration depth of a TDTR measurement (i.e., the depth at which the temperature falls to 1/e of that of the sample surface), δ, can be approximated as $\delta = \sqrt{\kappa/(\pi C_v f)}$, where κ and C_v are the thermal conductivity and volumetric heat capacity of the

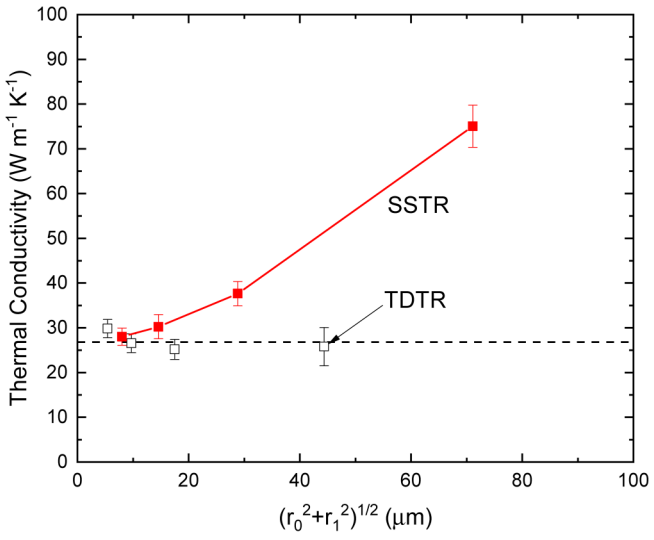

FIG. 3. Thermal conductivity measurements of the ion-implanted diamond as a function of effective spot radius assuming the sample to be a two-layered material system: an 80 nm film upon an ion-implanted diamond substrate, which is considered as a single continuum. Under this assumption, there is negligible change in measured thermal conductivity as a function of effective spot radius via TDTR measurements. In contrast, there is a strong correlation between effective spot radius and apparent thermal conductivity measured via SSTR.

medium.[8,9] The low thermal conductivity of the irradiated diamond in combination with the high modulation frequency of the pump beam restricts the thermal penetration depth to less than 1 μm of depth and, as such, the amorphous region is never sampled. As a quantitative example, a TDTR measurement utilizing a pump modulation frequency of 8.8 MHz on ion irradiated diamond, with an average thermal conductivity 26.8 W m^{-1} K^{-1} and volumetric heat capacity of 1.78 MJ m^{-3} K^{-1},[31] yields an estimated penetration depth of less than 0.74 μm. More accurate calculations of the thermal penetration depth (discussed later within this section) that account for the laser spot size and transducer/substrate interface result in a more conservative value. Thus, even with effective spot sizes as large as 44 μm, only the properties of the polycrystalline region above the amorphous band are sampled by the measurement. Therefore, accounting for the properties of the implanted region utilizing four layers (the aluminum transducer, the damaged polycrystalline diamond, the amorphous layer, and the pristine diamond) in the thermal model yields no change in the fitted thermal conductivity.

A slightly different approach to measure the thermal conductivity is applied with SSTR. In this case, a 532 nm continuous wave laser is mechanically chopped to induce a 400 Hz modulated heating event at the sample surface. The change in measured reflectance (ΔV) of a concentrically focused 786 nm probe is monitored as a function of the change in pump power (ΔP). As in the case of TDTR, SSTR measurements are taken with focusing objectives ranging from 20×-2× magnification. Examples of raw data (normalized by the measured DC probe signal, V) are shown in Fig. 2. Using the same two-layer representation of sample geometry, the thermal conductivity of the substrate is determined by modeling the system with a multi-layer heat diffusion model. We note that the uncertainty in the measurement is calculated in a similar manner as Braun *et al.*[32] and considers uncertainty attributed to the standard deviation in the calibration coefficient (γ) (which varies slightly depending upon the selected focusing objective used in the measurement), variance in the linear model, and also measurement repeatability. While γ is dependent upon a number of features within an optical setup, for reference, we note that values on the order of 1×10^7 were recorded in this study, with slight variations dependent upon the selected focusing objective. A single-crystal sapphire wafer was used in the determination of γ as its thermal conductivity was verified with TDTR and hot-disk transient plane source technique as 35 ± 2 W m^{-1} K^{-1}, which is similar in magnitude to the thermal conductivity of the damaged polycrystalline diamond (26.8 ± 2.1 W m^{-1} K^{-1}). Further details on the determination of γ are outlined in Ref. 32.

The results of the two-layer SSTR model for substrate thermal conductivity are plotted in Fig. 3. For small effective spot sizes (<10 μm), the fitted thermal conductivity of the second layer is in agreement with the measurements from TDTR. In contrast, the apparent increase in thermal conductivity observed for larger effective spot sizes illustrates that a two-layer-layer model is an inadequate representation of the physical geometry being probed by the SSTR measurement. In the event of steady-state laser heating, the depth of thermal penetration becomes limited by the laser spot size.[9,32] Therefore, as the radius of the effective spot size exceeds the depth of the amorphous layer, the underlying diamond substrate (which is unaffected by the ion implantation) is penetrated, yielding a higher apparent thermal conductivity if the amorphous layer is not accounted for in the thermal model, as we expand upon below.

For a more accurate representation of the sample geometry, the system is considered as a four-layer model: an 80 nm Al transducer, 7.03 μm of damaged diamond, and a 449 nm amorphous layer atop a polycrystalline substrate. Through four-point probe measurement and application of the Wiedemann–Franz law, the thermal conductivity of the Al layer is found to be 98 W m^{-1} K^{-1}. TDTR measurements of the thermal conductivity (26.8 W m^{-1} K^{-1}) and thermal boundary conductance (150 MW m^{-2} K^{-1}) are used to determine the properties of 7.03 μm of damaged diamond. For the third (amorphous) layer, the boundary conductances between the damaged diamond/amorphous layer and amorphous layer/pristine diamond are neglected, and the effective thermal conductivity is assumed to be on the order 1 W m^{-1} K^{-1}, which is an approximate value typical of amorphous materials,[33] including amorphous carbon.[34–37] The thermal conductivity of the substrate is also measured with TDTR (on an un-implanted sample) and found to be 1996 ± 213 W m^{-1} K^{-1}, reported previously.[11]

With this layer geometry, we gain insight into the model sensitivity to each layer parameter through the sensitivity analysis for each technique. The sensitivity is calculated as a function of effective spot size and displayed in Figs. 4(a) and 4(b) for SSTR and TDTR, respectively. For SSTR, the sensitivity is calculated in the method of Braun *et al.*[32] TDTR sensitivities are calculated using procedures from Gundrum *et al.*[38] For TDTR measurements [Fig. 4(b)], regardless of the spot size, the largest sensitivity is to the thermal conductivity of the damaged, polycrystalline region and to a lesser extent the Al/diamond interface. In the case of SSTR [Fig. 4(a)], for small spot sizes, there is high sensitivity to the thermal conductivity of Al and the damaged polycrystalline region. However, as the effective spot increases, there is a crossover in which the thermal conductivity of the amorphous layer dominates the measurement sensitivity.

The differences in sensitivity between the techniques can be largely attributed to the depths of thermal penetration. To illustrate this, the induced temperature rise of the aforementioned four-layer system is calculated for two heating scenarios using the same method as Refs. 11 and 32: the first assumes a 30 mW, 10 μm radius heat source modulated at 400 Hz and the second a 30 mW, 10 μm radius heat source modulated at 8.8 MHz to simulate the heating conditions in SSTR and TDTR, respectively. Two-dimensional temperature distributions are displayed in Figs. 4(c) and 4(d) for SSTR and TDTR, respectively, with the dashed green line displaying the 1/e thermal penetration depth. The corresponding cross-plane temperature distributions at the center location of the pump are displayed in Figs. 4(e) and 4(f). In the high-frequency heating case of TDTR, the temperature rise is localized near the surface, with a 1/e thermal penetration depth of less than 1 μm, and no temperature rise induced at depths beyond 4 μm. Correspondingly, there is no sensitivity to parameters beyond this depth. In the low-frequency heating limit, however, a temperature rise is induced throughout the entire depth of the amorphous layer, which is subsequently reduced at larger depths by the high thermal conductivity diamond substrate. This increased thermal penetration depth corresponds with

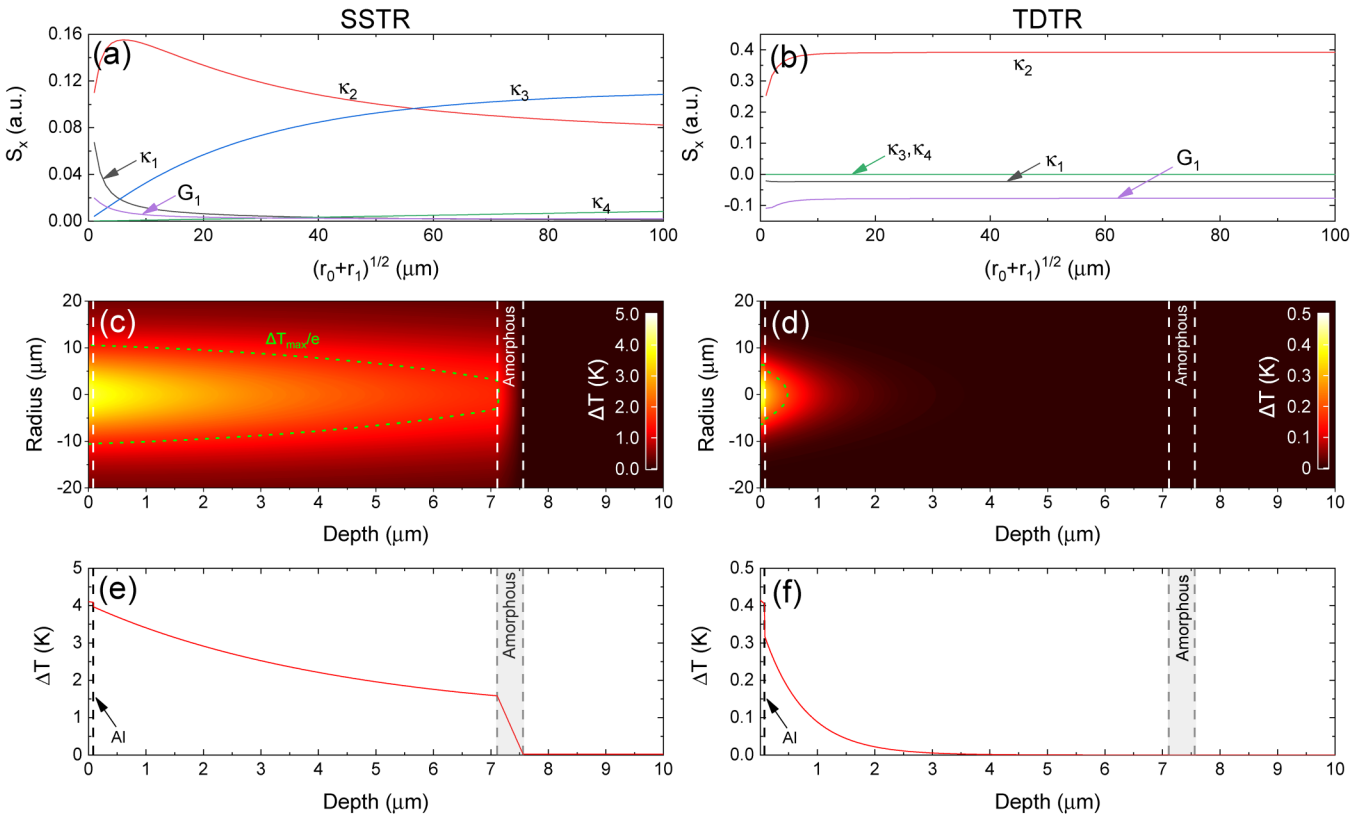

FIG. 4. Sensitivity analysis of the thermal properties of the implanted diamond by considering the sample as a four-layer system measured with SSTR (a) and TDTR (b). The subscripts refer to the corresponding layer in a top-down manner (for example, layer 1 refers to the Al transducer). Differences in sensitivity to a particular parameter between the two techniques are attributed to differences in thermal penetration depth. The expected temperature rise of the material system in response to a periodic heat source with frequency of 400 Hz (c) and 8.8 MHz (d) displays the difference in the heating profile of SSTR and TDTR. Both calculations apply a pump and probe radius of 10 μm; while the temperature rise of an 8.8 MHz modulated heating event is primarily contained within the 80 nm transducer, a 400 Hz periodic heating event yields a 1/e thermal penetration depth capable of extending to the amorphous layer. The temperature profile at the center of the pump/probe radius is displayed in (e) and (f).

enhanced sensitivity to parameters at larger depths, as seen in Fig. 4(a), including the amorphous layer.

As sensitivity analysis and calculations of the thermal penetration depth indicate sensitivity to the thermal conductivity of the amorphous layer in the low frequency limit, the ΔV/V SSTR measurements are analyzed as the four-layer geometry described previously. The properties of the Al, damaged polycrystalline diamond region, and pristine diamond are obtained through four-point probe measurements and TDTR, and the thermal conductivity of the amorphous layer is then treated as a fitting parameter within the multi-layer heat diffusion model[32] of the measured data. The thermal conductivity of the amorphous layer is plotted as a function of effective spot size in Fig. 5(a). In contrast to the two-layer fitting from Fig. 3, the conductivity is more consistent as a function of effective spot size, with nominal values within error of the other measurements and an average thermal conductivity of $1.4 \pm 0.4\ \mathrm{W\,m^{-1}\,K^{-1}}$.

To assess the result of the measurement and the ability of the technique to measure amorphous films, the thermal conductivity of the amorphous diamond layer is compared to that of amorphous carbon films fabricated with controlled growth and thickness. In particular, a series of diamond-like carbon (DLC) films were fabricated through plasma enhanced chemical vapor deposition (PECVD)[34,39] upon 300 mm diameter Si (001) substrates with a thickness range of 24–500 nm. While the films are amorphous in structure, the designation of diamond-like specifies a higher ratio of sp^3:sp^2 bonding than that typically found in PECVD grown amorphous carbon.[35–37,39–41]

The thermal conductivity of the DLC films was first measured through TDTR, using a modulation frequency of 8.8 MHz and a 10× objective, providing for an effective spot size of 9.7 μm. As in the case of the irradiated diamond, the DLC films were coated with an 80 nm layer of Al to serve as the transducer. Measurements of a witness sample yielded a thermal conductivity of $123 \pm 8\ \mathrm{W\,m^{-1}\,K^{-1}}$ for the silicon substrate. For measurements of the DLC films, the thermal conductivity of the film and the thermal boundary conductance of the Al/DLC film interface were treated as fitting parameters. The thermal boundary conductance

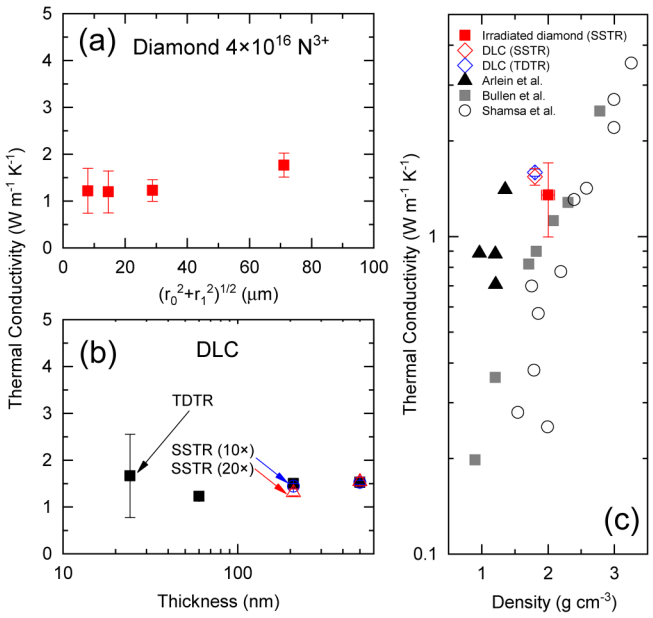

FIG. 5. (a) Measured thermal conductivity of the amorphous region (κ_3) of the ion-implanted diamond sample, considering the material system as a four-layer model. (b) Measured thermal conductivity of amorphous carbon in a thickness series of diamond-like carbon films. (c) Thermal conductivity of amorphous carbon as measured with TDTR and SSTR. For reference, experimental values are included from literature as a function of density,[34–36] originally compiled in a work by Arlein *et al.*[34] Reproduced from Arlein *et al.*, J. Appl. Phys. **104**, 033508 (2008). Copyright 2008 AIP Publishing LLC.

of the DLC film/substrate was treated as infinite as there was little sensitivity to the interface. Results of the DLC measurements are displayed in Fig. 5(b); in general, the thermal conductivity was found to be relatively constant within the measured thickness range with an average of $1.5 \pm 0.2\ \mathrm{W\,m^{-1}\,K^{-1}}$, which is in close comparison to the thermal conductivity of the amorphous layer within the irradiated diamond. For comparison, SSTR was also used (with 10× and 20× objectives) to measure the thermal conductivity of the PECVD DLC films. For the two thinnest films of 24 and 60 nm, there was little sensitivity to the thermal conductivity of the films; however, results could be obtained on thicker films (>100 nm) and were found to be within good agreement (<12% difference) of the TDTR measurements, as shown in Fig. 5(b).

Despite the similarity in the measured thermal conductivity of the amorphous diamond layer and amorphous PECVD carbon films, it is important to note that the thermal conductivity of amorphous carbon has been shown to be highly dependent upon film density.[35–37,40,41] This is closely linked to the type of bonding most prevalent to the film. For example, a higher fraction of C–C sp^3 bonds (as compared to H-terminated bonds) provides for enhanced stiffness and density. For these films, the corresponding thermal conductivity has been shown to span over an order of magnitude, ranging from less than $1\ \mathrm{W\,m^{-1}\,K^{-1}}$ to nearly $10\ \mathrm{W\,m^{-1}\,K^{-1}}$, depending upon the density. For reference, we plot the reported thermal conductivities of amorphous carbon films from Arlein *et al.*,[34] Bullen *et al.*,[36] and Shamsa *et al.*[35] as a function of film density in Fig. 5(c). The density of the PECVD films in this study was measured with Rutherford backscattering spectrometry (RBS) analysis ($1.8\ \mathrm{g\,cm^{-3}}$). The corresponding thermal conductivity of $1.5\ \mathrm{W\,m^{-1}\,K^{-1}}$ is within the range of that from amorphous carbon films from the literature with similar density.

We find this correlation between density and thermal conductivity to also be applicable for amorphous carbon produced through ion irradiation of diamond. For example, in a prior report by Fairchild *et al.*,[13] the formation of an amorphous band was likewise observed in diamond following implantation with He^+ at 0.5 MeV. A threshold density value of $2.95\ \mathrm{g\,cm^{-3}}$ was determined, below which amorphization was found to occur. Within the amorphous band, densities ranging from 2.95 to $2.1\ \mathrm{g\,cm^{-3}}$ were observed. With an average value of $2.53\ \mathrm{g\,cm^{-3}}$, a thermal conductivity of $1.39\ \mathrm{W\,m^{-1}\,K^{-1}}$ could be interpolated from the data of Shamsa *et al.*[35] and $1.85\ \mathrm{W\,m^{-1}\,K^{-1}}$ from Bullen *et al.*,[36] which is within the range of the thermal conductivity of the irradiation-induced amorphous carbon of the present study.

For insight into the density of the amorphous region in the present study, electron energy loss spectroscopy (EELS) analysis was performed, from which shifts in the peak of the plasmon spectrum were used to calculate the density from a cross section of the sample. Specifics on the density calculations are elaborated on in the supplementary material. Maps of the plasmon peak position could then be used to provide visualization of the spatial density variation, such as that shown in Fig. 6, where a density map 6(b) is contrasted to the corresponding HAADF STEM image 6(a). From this analysis, the density of the damaged region pre-end-of-range was found to be approximately $3.4\ \mathrm{g\,cm^{-3}}$, whereas the amorphous layer was reduced to a density ranging from 1.9 to $2.1\ \mathrm{g\,cm^{-3}}$. For comparison, the thermal conductivity of the amorphous carbon induced through ion implantation is plotted with the PECVD amorphous carbon films in Fig. 5(c). In general, the thermal conductivity is in agreement with amorphous carbon films fabricated through PECVD, which serves to highlight the critical role of density in dictating the thermal conductivity of carbon and also lends credence to the measurement.

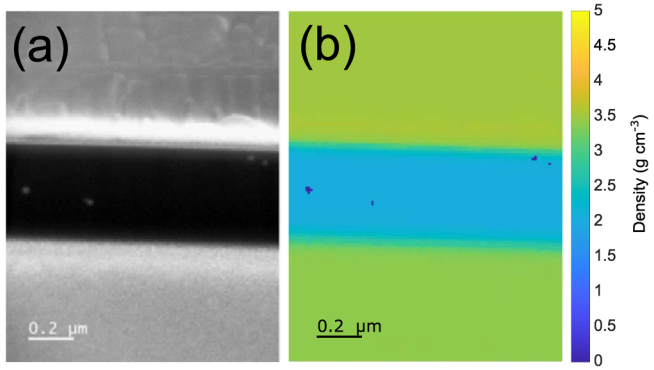

FIG. 6. (a) HAADF STEM image of an FIB cross section of the irradiated diamond. (b) displays the corresponding spatially resolved density of the region as determined from the EELS analysis.

IV. SUMMARY

In summary, we report on the thermal conductivity of an amorphous carbon layer generated in diamond via high energy N^{3+} implantation. While TDTR measurements provide insight into the thermal conductivity of the region preceeding the projected range, the high frequency of the measurement limits the depth of thermal penetration, thereby inhibiting the ability to probe the amorphous band. To enhance sensitivity to the region, SSTR is employed which utilizes lower frequencies of modulation and heats the sample into a steady-state regime, in which the depth of thermal penetration is spot size limited. Through measurement with a series of objective lenses, we find the thermal conductivity of the amorphous region to be $1.4 \pm 0.4\,\mathrm{W\,m^{-1}\,K^{-1}}$, which is comparable to amorphous carbon films of similar density ($1.9–2.1\,\mathrm{g\,cm^{-3}}$). The enhanced thermal penetration depths achievable with SSTR provide for new opportunities to probe regions beyond those which could traditionally be probed with thermoreflectance techniques.

SUPPLEMENTARY MATERIAL

See the supplementary material for additional information on density determination and EELS analysis.

ACKNOWLEDGMENTS

This material is based upon work supported by the Air Force Office of Scientific Research under Award No. FA9550-18-1-0352. We appreciate support from the Office of Naval Research through a MURI program, Grant No. N00014-18-1-2429. This work was performed, in part, at the Center for Integrated Nanotechnologies, an Office of Science User Facility operated for the U.S. Department of Energy (DOE) Office of Science. Sandia National Laboratories is a multimission laboratory managed and operated by National Technology & Engineering Solutions of Sandia, LLC, a wholly owned subsidiary of Honeywell International Inc., for the U.S. Department of Energy's National Nuclear Security Administration under Contract No. DE-NA0003525. This paper describes objective technical results and analysis. Any subjective views or opinions that might be expressed in the paper do not necessarily represent the views of the U.S. Department of Energy or the United States Government.

DATA AVAILABILITY

The data that support the findings of this study are available from the corresponding author upon reasonable request.

REFERENCES

[1]P. Jiang, X. Qian, and R. Yang, "Tutorial: Time-domain thermoreflectance (TDTR) for thermal property characterization of bulk and thin film materials," J. Appl. Phys. **124**, 161103 (2018).
[2]D. H. Olson, J. L. Braun, and P. E. Hopkins, "Spatially resolved thermoreflectance techniques for thermal conductivity measurements from the nanoscale to the mesoscale," J. Appl. Phys. **126**, 150901 (2019).
[3]D. G. Cahill, "Analysis of heat flow in layered structures for time-domain thermoreflectance," Rev. Sci. Instrum. **75**, 5119–5122 (2004).
[4]A. Giri and P. E. Hopkins, "A review of experimental and computational advances in thermal boundary conductance and nanoscale thermal transport across solid interfaces," Adv. Funct. Mater. **30**, 1903857 (2020).
[5]J. T. Gaskins, G. Kotsonis, A. Giri, S. Ju, A. Rohskopf, Y. Wang, T. Bai, E. Sachet, C. T. Shelton, Z. Liu, Z. Cheng, B. M. Foley, S. Graham, T. Luo, A. Henry, M. S. Goorsky, J. Shiomi, J.-P. Maria, and P. E. Hopkins, "Thermal boundary conductance across heteroepitaxial ZnO/GaN interfaces: Assessment of the phonon gas model," Nano Lett. **18**, 7469–7477 (2018).
[6]E. A. Scott, J. T. Gaskins, S. W. King, and P. E. Hopkins, "Thermal conductivity and thermal boundary resistance of atomic layer deposited high-k dielectric aluminum oxide, hafnium oxide, and titanium oxide thin films on silicon," APL Mater. **6**, 058302 (2018).
[7]E. A. Scott, S. W. Smith, M. D. Henry, C. M. Rost, A. Giri, J. T. Gaskins, S. S. Fields, S. T. Jaszewski, J. F. Ihlefeld, and P. E. Hopkins, "Thermal resistance and heat capacity in hafnium zirconium oxide ($Hf1–xZrxO_2$) dielectrics and ferroelectric thin films," Appl. Phys. Lett. **113**, 192901 (2018).
[8]Y. K. Koh and D. G. Cahill, "Frequency dependence of the thermal conductivity of semiconductor alloys," Phys. Rev. B **76**, 075207 (2007).
[9]J. L. Braun and P. E. Hopkins, "Upper limit to the thermal penetration depth during modulated heating of multilayer thin films with pulsed and continuous wave lasers: A numerical study," J. Appl. Phys. **121**, 175107 (2017).
[10]J. L. Braun, C. J. Szwejkowski, A. Giri, and P. E. Hopkins, "On the steady-state temperature rise during laser heating of multilayer thin films in optical pump–probe techniques," J. Heat Transfer **140**, 052801 (2018).
[11]E. A. Scott, K. Hattar, J. L. Braun, C. M. Rost, J. T. Gaskins, T. Bai, Y. Wang, C. Ganski, M. Goorsky, and P. E. Hopkins, "Orders of magnitude reduction in the thermal conductivity of polycrystalline diamond through carbon, nitrogen, and oxygen ion implantation," Carbon **157**, 97–105 (2020).
[12]S. Rubanov, B. A. Fairchild, A. Suvorova, P. Olivero, and S. Prawer, "Structural transformation of implanted diamond layers during high temperature annealing," Nucl. Instrum. Methods Phys. Res. Sect. B **365**, 50–54 (2015).
[13]B. A. Fairchild, S. Rubanov, D. W. M. Lau, M. Robinson, I. Suarez-Martinez, N. Marks, A. D. Greentree, D. McCulloch, and S. Prawer, "Mechanism for the amorphisation of diamond," Adv. Mater. **24**, 2024–2029 (2012).
[14]P. Olivero, S. Rubanov, P. Reichart, B. C. Gibson, S. T. Huntington, J. Rabeau, A. D. Greentree, J. Salzman, D. Moore, D. N. Jamieson, and S. Prawer, "Ion-beam-assisted lift-off technique for three-dimensional micromachining of freestanding single-crystal diamond," Adv. Mater. **17**, 2427–2430 (2005).
[15]J. F. Ziegler, "High energy ion implantation," Nucl. Instrum. Methods Phys. Res. Sect. B **6**, 270–282 (1985).
[16]J. F. Ziegler, M. D. Ziegler, and J. P. Biersack, "SRIM—The stopping and range of ions in matter (2010)," Nucl. Instrum. Methods Phys. Res. Sect. B **268**, 1818–1823 (2010).
[17]J. Koike, D. M. Parkin, and T. E. Mitchell, "Displacement threshold energy for type IIa diamond," Appl. Phys. Lett. **60**, 1450–1452 (1992).
[18]J. C. Bourgoin and B. Massarani, "Threshold energy for atomic displacement in diamond," Phys. Rev. B **14**, 3690–3694 (1976).
[19]R. Q. Hood, P. R. C. Kent, R. J. Needs, and P. R. Briddon, "Quantum Monte Carlo study of the optical and diffusive properties of the vacancy defect in diamond," Phys. Rev. Lett. **91**, 076403 (2003).
[20]P. R. C. Kent, M. D. Towler, R. J. Needs, and G. Rajagopal, "Carbon clusters near the crossover to fullerene stability," Phys. Rev. B **62**, 15394–15397 (2000).
[21]H. Shin, S. Kang, J. Koo, H. Lee, J. Kim, and Y. Kwon, "Cohesion energetics of carbon allotropes: Quantum Monte Carlo study," J. Chem. Phys. **140**, 114702 (2014).
[22]Y. S. Nechaev and T. N. Veziroglu, "Thermodynamic aspects of the graphene/graphane/hydrogen systems: Relevance to the hydrogen on-board storage problem," Adv. Mater. Phys. Chem. **3**, 255–280 (2013).
[23]Y. S. Nechaev, V. P. Filippova, A. Yürüm, Y. Yürüm, and N. Veziroğlu, "The reversible hydrogenation-dehydrogenation of membrane and epitaxial graphenes," J. Chem. Eng. Chem. Res. **2**, 421–456 (2015), available at https://research.sabanciuniv.edu/29103/.
[24]S. Prussin, D. I. Margolese, and R. N. Tauber, "Formation of amorphous layers by ion implantation," J. Appl. Phys. **57**, 180–185 (1985).

[25]E. A. Scott, K. Hattar, C. M. Rost, J. T. Gaskins, M. Fazli, C. Ganski, C. Li, T. Bai, Y. Wang, K. Esfarjani, M. Goorsky, and P. E. Hopkins, "Phonon scattering effects from point and extended defects on thermal conductivity studied via ion irradiation of crystals with self-impurities," Phys. Rev. Mater. **2**, 095001 (2018).
[26]F. Bosia, N. Argiolas, M. Bazzan, B. A. Fairchild, A. D. Greentree, D. W. M. Lau, P. Olivero, F. Picollo, S. Rubanov, and S. Prawer, "Direct measurement and modelling of internal strains in ion-implanted diamond," J. Phys. Condens. Matter **25**, 385403 (2013).
[27]N. R. Parikh, J. D. Hunn, E. McGucken, M. L. Swanson, C. W. White, R. A. Rudder, D. P. Malta, J. B. Posthill, and R. J. Markunas, "Single-crystal diamond plate liftoff achieved by ion implantation and subsequent annealing," Appl. Phys. Lett. **61**, 3124–3126 (1992).
[28]M. Nastasi, J. W. Mayer, and Y. Wang, *Ion Beam Analysis: Fundamentals and Applications* (CRC Press, 2014).
[29]R. E. Stoller, M. B. Toloczko, G. S. Was, A. G. Certain, S. Dwaraknath, and F. A. Garner, "On the use of SRIM for computing radiation damage exposure," Nucl. Instrum. Methods Phys. Res. Sect. B **310**, 75–80 (2013).
[30]H. Paul and A. Schinner, "Judging the reliability of stopping power tables and programs for protons and alpha particles using statistical methods," Nucl. Instrum. Methods Phys. Res. Sect. B **227**, 461–470 (2005).
[31]J. E. Desnoyehs and J. A. Morrison, "The heat capacity of diamond between 12·8 and 277 k," Philos. Mag. J. Theor. Exp. Appl. Phys. **3**, 42–48 (1958).
[32]J. L. Braun, D. H. Olson, J. T. Gaskins, and P. E. Hopkins, "A steady-state thermoreflectance method to measure thermal conductivity," Rev. Sci. Instrum. **90**, 024905 (2019).
[33]J. J. Freeman and A. C. Anderson, "Thermal conductivity of amorphous solids," Phys. Rev. B **34**, 5684–5690 (1986).
[34]J. L. Arlein, S. E. M. Palaich, B. C. Daly, P. Subramonium, and G. A. Antonelli, "Optical pump-probe measurements of sound velocity and thermal conductivity of hydrogenated amorphous carbon films," J. Appl. Phys. **104**, 033508 (2008).
[35]M. Shamsa, W. L. Liu, A. A. Balandin, C. Casiraghi, W. I. Milne, and A. C. Ferrari, "Thermal conductivity of diamond-like carbon films," Appl. Phys. Lett. **89**, 161921 (2006).
[36]A. J. Bullen, K. E. O'Hara, D. G. Cahill, O. Monteiro, and A. von Keudell, "Thermal conductivity of amorphous carbon thin films," J. Appl. Phys. **88**, 6317–6320 (2000).
[37]C. J. Morath, H. J. Maris, J. J. Cuomo, D. L. Pappas, A. Grill, V. V. Patel, J. P. Doyle, and K. L. Saenger, "Picosecond optical studies of amorphous diamond and diamondlike carbon: Thermal conductivity and longitudinal sound velocity," J. Appl. Phys. **76**, 2636–2640 (1994).
[38]B. C. Gundrum, D. G. Cahill, and R. S. Averback, "Thermal conductance of metal-metal interfaces," Phys. Rev. B **72**, 245426 (2005).
[39]G. A. Antonelli, S. Reddy, P. Subramonium, J. Henri, J. Sims, J. O'loughlin, N. Shamma, D. Schlosser, T. Mountsier, W. Guo, and H. Sawin, "Patterning with amorphous carbon thin films," ECS Trans. **35**, 701 (2011).
[40]H. Harikrishna, W. A. Lanford, S. W. King, and S. T. Huxtable, "Thermal conductivity of plasma deposited amorphous hydrogenated boron and carbon rich thin films," J. Nucl. Mater. **514**, 154–160 (2019).
[41]Y. Young Kim, H. Adli Alwi, R. Awang, and S. Krishnaswamy, "Influence of radio frequency power on thermal diffusivity of plasma enhanced chemical vapor deposition-grown hydrogenated amorphous carbon thin-films," J. Appl. Phys. **109**, 113503 (2011).